ORIGINAL ARTICLE

Computed tomography and photoacoustic imaging guided photodynamic therapy against breast cancer based on mesoporous platinum with *insitu* oxygen generation ability

Lingyan Zhang[a,b], Mifang Li[b], Quan Zhou[b], Meng Dang[c], Yuxia Tang[a], Shouju Wang[d], Jijun Fu[e], Zhaogang Teng[c,*], Guangming Lu[a,*]

[a]*Department of Medical Imaging, Jinling Hospital, The First School of Clinical Medicine, Southern Medical University, Nanjing 210002, China*
[b]*Department of Medical Imaging, The Third Affiliated Hospital, Southern Medical University, Guangzhou 510630, China*
[c]*Key Laboratory for Organic Electronics & Information Displays and Institute of Advanced Materials, Jiangsu Key Laboratory for Biosensors, Jiangsu National Synergetic Innovation Centre for Advanced Materials, Nanjing University of Posts and Telecommunications, Nanjing 210046, China*
[d]*Department of Medical Imaging, Jiangsu Province Hospital, Nanjing 210029, China*
[e]*Key Laboratory of Molecular Target & Clinical Pharmacology, School of Pharmaceutical Sciences, Guangzhou Medical University, Guangzhou 511436, China*

Abstract Photodynamic therapy (PDT) has been widely used in cancer treatment. However, hypoxia in most solid tumors seriously restricts the efficacy of PDT. To improve the hypoxic microenvironment, we designed a novel mesoporous platinum (mPt) nanoplatform to catalyze hydrogen peroxide (H_2O_2) within the tumor cells *in situ* without an extra enzyme. During the fabrication, the carboxy terminus of the photosensitizer chlorin e6 (Ce6) was connected to the amino terminus of the bifunctional mercaptoaminopolyglycol (SH-PEG-NH$_2$) by a condensation reaction, and then PEG-Ce6 was modified onto the mPt moiety *via* the mercapto terminal of SH-PEG-NH$_2$. Material, cellular and animal experiments demonstrated that Pt@PEG-Ce6 catalyzed H_2O_2 to produce oxygen (O_2) and that Ce6 transformed O_2 to

generate reactive oxygen species (ROS) upon laser irradiation. The Pt@PEG-Ce6 nanoplatform with uniform diameter presented good biocompatibility and efficient tumor accumulation. Due to the high atomic number and good near-infrared absorption for Pt, this Pt@PEG-Ce6 nanoplatform showed computed tomography (CT) and photoacoustic (PA) dual-mode imaging ability, thus providing an important tool for monitoring the tumor hypoxic microenvironment. Moreover, the Pt@PEG-Ce6 nanoplatform reduced the expression of hypoxia-inducible factor-1α (HIF-1α) and programmed death-1 (PD-1) in tumors, discussing the relationship between hypoxia, PD-1, and PDT for the first time.

1. Introduction

Surgical treatment, radiotherapy, chemotherapy, and biological treatment are common treatment methods for tumors. However, traditional therapies are generally accompanied by invasiveness, side effects and low selectivity. Currently, photodynamic therapy (PDT) has been recognized as an accurate and noninvasive treatment method for tumors[1,2]. During PDT treatment, reactive oxygen species (ROS) are generated *via* the reaction of the photosensitizer with tissue oxygen, which can kill tumor cells and destroy tumor blood vessels. However, hypoxia easily occurs during the growth of tumor cells, thus inducing resistance of the tumors to PDT[3−7]. Therefore, solving the problem of hypoxia has become increasingly important to improve the PDT efficacy in tumors.

A variety of strategies have been developed to treat tumor hypoxia and improve the efficacy of PDT[7,8], including hyperbaric oxygen therapy[9], antitumor angiogenesis therapy[10], biological reduction therapy[11], and oxygen transport or generation *via* nanomaterials[12,13]. Recently, an *in situ* catalytic strategy using nanomaterials to overcome tumor hypoxia has become one of the most promising research directions[14−16]. One *in situ* catalytic nanomaterial, manganese oxide (MnO_2), can decompose to produce oxygen in the acidic environment of the tumor to improve the efficiency of PDT, but the synthesis procedures are complex[17−19]. Noble metal Pt is an important kind of oxygen-producing nanomaterial with high catalytic activity[20−25]. In addition, Pt has the ability for computed tomography (CT) and photoacoustic (PA) imaging due to its high atomic number and good near infrared absorption[26]. However, Pt nanoparticles generally do not have pores; thus, it is difficult to load drugs into them for tumor treatment[27,28]. To address these deficiencies and problems, we assumed that mesoporous platinum (mPt) nanoparticles with abundant pores may significantly increase the specific surface area and improve oxygen production and drug loading ability[29−31]. Accordingly, we constructed an integrated and biocompatible mesoporous Pt-based PDT nanoplatform *via* connecting the polyethylene glycol-modified photosensitizer chlorin e6 (Ce6) onto the mesoporous Pt nanoparticles (denoted as Pt@PEG-Ce6). The mesoporous structure of Pt endows it with a high loading capacity for photosensitizers. Moreover, Pt can effectively catalyze H_2O_2 to O_2, which sequentially receives the energy transferred by Ce6 from lasers to generate singlet oxygen ($^1O_2$) for PDT. Furthermore, Pt@PEG-Ce6 has the characteristics of CT and PA imaging, which provides good tracking for the visualization of tissue distribution and enhances the signal of the tumor. Mouse tumor immunohistochemistry analysis indicated that the Pt@PEG-Ce6 nanoplatform not only reduces the expression of hypoxia-inducible factor-1α (HIF-1α) but also directly reduces the expression of programmed death-1 (PD-1) on the surface of T-cells. The decrease in PD-1 inhibits its combination with programmed death ligand-1 (PD-L1) on the surface of cancer cells. Therefore, the apoptosis of T cells reduced and activated the tumor-killing effect of immune effector cells[32]. To the best of our knowledge, this is the first study to discuss the relationship between hypoxia, PD-1, and PDT, laying an experimental foundation for further exploration of the role of this nanoplatform in tumor treatment.

2. Materials and methods

2.1. Materials

All chemicals were obtained from commercial suppliers. Pluronic F127 (PF127), potassium bromide (KBr), ascorbic acid (AA) and chloroplatinic acid were obtained from Sinopharm Chemical Reagent Co., Ltd. (Shanghai, China). Photosensitizer chlorin e6 (Ce6) was purchased from Dalian Meilun Biotechnology Co., Ltd. (Dalian, China). 1-Ethyl-3-[3-dimethylaminopropyl]carbodiimide hydrochloride (EDC), *N*-hydroxysuccinimide (NHS) and 1,3-diphenylisobenzofuran (DPBF) were purchased from Aladdin Co., Ltd. (Shanghai, China). Mercaptoaminopolyglycol (SH-PEG-NH_2), cell counting kit-8 (CCK-8) and 4′,6-diamidino-2-phenylindole (DAPI) were obtained from Keygen Biotech Co., Ltd. (Nanjing, China). 2′,7′-Dichlorofluorescein diacetate (DCFH-DA) was purchased from Thermo Fisher Scientific Co., Ltd. (Shanghai, China). Hypoxia inducible factor-1 (HIF-1α) and programmed death ligand-1 (PD-1) antibodies were purchased from Bioss Antibodies Co., Ltd. (Beijing, China).

2.2. Characterization

The sizes and morphologies of the nanoparticles were determined by a high-resolution transmission electron microscope (HRTEM, JEOL, JEM-2100, Tokyo, Japan) and a scanning electron microscope (SEM, Hitachi S-4800, Tokyo, Japan). UV−Vis absorption spectra were measured on an ultraviolet−Visible spectrophotometer (Shimadzu, UV2600, Kyoto, Japan). Zeta potential and DLS were carried out on a Zetasizer Nano (Malvern Instruments, Zetasizer Nano ZS, Malvern, UK). CCK-8 experiments were carried out on an ELISA (Biotek, Synergy HTX, Winooski, VT, USA). Flow cytometry analysis was taken with a flow cytometry (Beckman coulter, CytoFLEX, Brea, CA, USA). FT-IR spectra

were obtained using a spectrometer (Nicolet Instruments, Nicolet Nexus 870, Madison, WI, USA). Pathological images were taken with an Upright Metallurgical Microscope (Carl Zeiss, Axio Imager A2, Jena, Germany). A 660 nm laser (OXLasers Electronics Co., Ltd., OX-MZ650L, Shanghai, China) were used to perform photodynamic therapy.

2.3. Synthesis of Pt@PEG-Ce6

2.3.1. Synthesis of the Pt nanomaterials
PF127 (900 mg), KBr (2000 mg), AA (0.1 mol/L, 30 mL) were dissolved in H_2O (25 mL) using ultrasonication. Then, 1.5 mL of chloroplatinic acid (0.2 mol/L) was added to the above seed solution under static reaction conditions for 15 h at 70 °C. Then, the particles were collected by centrifugation (Beckman coulter, Avanti J-15, Brea, CA, USA, 8000 rpm, 10 min) and washed three times with ethanol. The prepared Pt nanomaterials were dispersed in 100 mL of ethanol and 200 μL of concentrated hydrochloric acid for 10 min using ultrasonication and then stirred for 3 h with a magnetic stirrer (KEWLAB, Hangzhou, China, 500 rpm) at 60 °C to remove the surfactant PF127 on the surface of the Pt nanoparticles. Subsequently, the particles were collected by centrifugation (Beckman coulter, 8000 rpm, 10 min) and washed three times with ethanol. The mPt nanomaterials were prepared and stored in 40 mL of ethanol solution.

2.3.2. Synthesis of PEG-Ce6 nanomaterials
A mixed solution containing Ce6 (0.5 mg), EDC (0.6 mg), NHS (0.7 mg) and water (1.8 mL) was shaken at room temperature for 4 h to activate Ce6. After the addition of the $SH-PEG-NH_2$ solution (2 mg/mL, 1 mL) to the activated Ce6 and reacting together with shaking at room temperature for 12 h, the PEG-Ce6 nanomaterials were made.

2.3.3. Synthesis of Pt@PEG-Ce6 nanomaterials
The resultant mPt nanomaterials were centrifuged (Beckman coulter, 8000 rpm, 10 min) and washed three times with pure water. Then, 1 mL of pure water was added to the mPt solution, which was dispersed with ultrasound for several minutes. Subsequently, the mPt solution was added to the synthesized PEG-Ce6 solution, and the reaction was carried out in a shaker at room temperature for 2 h. The above particles were collected by centrifugation (Beckman coulter, 8000 rpm, 10 min) and washed three times with pure water, repeating the above steps three times. The final obtained Pt@PEG-Ce6 was dispersed in water.

2.4. CT imaging and photoacoustic imaging of the nanomaterials

The mPt nanomaterials were diluted into different concentration gradients (0, 50, 100, 200, 400 and 600 μg/mL) and dispersed in a 1% agar mixture. All samples were placed in test tubes using a clinical dual-source CT imaging system (Siemens, Somatom Definition, Berlin, Germany) to scan. The CT imaging parameters were as follows: slice thickness, 5 mm; voltage, 120 kV; electricity, 420 mA; matrix, 512 × 512. Cross-sectional images of all captured samples were transmitted to specialized workstations (multimodal workplaces, Berlin, Germany) to quantify the X-ray attenuation of the regions of interest (ROIs). The center of each cross-section was taken as the ROI, and the CT value of each sample was measured three times to determine its average value as the final CT value. In addition, Pt@PEG-Ce6 nanomaterials were diluted to different concentrations (0.5, 0.25 and 0.125 mg/mL) and filled in plastic tubes, and then placed in the photoacoustic microscopy imager (Made by South China normal university, Guangzhou, China) for scanning. The laser wavelength of the photoacoustic imager was 532 nm.

2.5. Catalase activity detection of the Pt@PEG-Ce6 nanocomposite

An oxygen probe (JPBJ-608 Portable Dissolved Oxygen Meter, Leici, Shanghai, China) was used to measure O_2 to compare the catalase activity of Pt@PEG-Ce6. mPt, Ce6 and Pt@PEG-Ce6 were dispersed in water containing 10 μL of H_2O_2, and the oxygen concentrations of H_2O, H_2O_2, $Pt+H_2O_2$, $Pt@PEG-Ce6+H_2O_2$ and $Ce6+H_2O_2$ were detected by a dissolved oxygen meter.

2.6. Singlet oxygen generation by the Pt@PEG-Ce6 nanocomposite

1,3-Diphenylisobenzofuran (DPBF) was selected as a probe to detect the generation of singlet oxygen from the Pt@PEG-Ce6 nanocomposite in the presence or absence of H_2O_2 upon 660 nm laser irradiation. 10 μL DPBF (1 mg/mL, dissolved in acetonitrile) was added to both free Ce6 and Pt@PEG-Ce6 with or without 10 μL H_2O_2. The final concentration of Ce6 was 10 μg/mL. In the presence or absence of H_2O_2, the absorbance and absorption curve of each group solution at 410 nm were measured by ultraviolet–Visible spectrophotometer under different times of laser irradiation (660 nm, 1 W/cm^2).

2.7. Cytotoxicity of the Pt@PEG-Ce6 nanocomposite

4T1 and MCF-7/ADR (dox-resistant) cells were inoculated into 96-well plates (1 × 10^5 cells per well) and incubated at 37 °C and 5% CO_2 for 24 h. Then, Pt@PEG-Ce6 or mPt at different concentrations (0, 5, 10, 20, 40, or 80 ppm) were added and incubated for an additional 24 h. Then, CCK8 (10 μL) was added and incubated for an additional 0.5 h. Finally, the absorbance was recorded at 490 nm using an ELISA to analyze the cytotoxicity of the nanomaterials by comparing the relative viability of the cells between the experimental group and the control group.

2.8. Enhancement of PDT in cell levels by Pt@PEG-Ce6

4T1 and MCF-7/ADR (dox-resistant) cells were inoculated into 96-well plates (1 × 10^5 cells per well) and incubated at 37 °C and 5% CO_2 for 24 h. Then, Pt@PEG-Ce6 or free Ce6 at different concentrations (20 or 50 ppm) were added and incubated for an additional 24 h. After washing the cells with phosphate-buffered saline (PBS) three times to remove the superfluous nanoparticles or photosensitizers, serum-free medium containing 10×10^{-6} mol/L singlet oxygen detection probe 2′,7′-dichlorofluorescein diacetate (DCFH-DA) was added and incubated in an air (37 °C, 5% CO_2 incubator) or nitrogen (100% nitrogen and 0% oxygen incubator) atmosphere for 30 min. Then, the cells were washed twice with PBS to remove the excess DCFH-DA and were irradiated with a laser (660 nm, 1 W/cm^2) for 10 min per well. Finally, flow cytometry analysis was performed to analyze the cells.

2.9. Biosafety assessment of the Pt@PEG-Ce6 nanocomposite

Female BALB/c mice (5 weeks old) were purchased from the Southern Medical University Laboratory Animal Center (Guangzhou, China). Animal work was performed under protocols approved by the Institutional Animal Care and Use Committee. Mice were randomly divided into the experimental group and the control group, and the experimental group was injected with Pt@PEG-Ce6 (1 mg/mL, 100 μL) *via* the tail vein, and the control group was injected with saline (100 μL). Blood was collected from the experimental group and the control group 24 h after the injection, and the blood biochemical analysis was conducted. Meanwhile, the hearts, livers, spleens, lungs, and kidneys of the mice were collected for histological analysis.

2.10. Animal model establishment

A mouse breast cancer subcutaneous tumor model was used with the 4T1 cell line. After the cells were cultured to a certain amount, the cells were digested by trypsin and washed three times with PBS to disperse in PBS. A 50 μL cell (1×10^7 cells) dispersion was inoculated subcutaneously in the right posterior of each BALB/c mouse body, and the following experiments were performed when the tumor size reached 100 mm^3.

2.11. In vivo CT and photoacoustic imaging

After the establishment of a tumor-bearing mouse model, the 128-layer spiral CT (Toshiba, Japan) was used to perform CT scanning on the mice. The CT imaging parameters were as follows: slice thickness, 1.0 mm; voltage, 120 kV; electricity, 300 mA; matrix, 512×512. Following intravenous injection of Pt@PEG-Ce6 (1 mg/mL, 100 μL), the mice were scanned again 15 min after the injection. In addition, a photoacoustic microscopy imager (Made by South China Normal University) and a photoacoustic tomography imager (VisualSonics, Vevo LAZR, Toronto, Canada) were used to perform photoacoustic scanning on the mice. After intravenous injection of Pt@PEG-Ce6 (1 mg/mL, 100 μL) for 4 h, the tumor region of each mouse received laser irradiation (660 nm, 1 W/cm) for 5 min. Then, the mice were scanned again 1 day later. The laser wavelength of the photoacoustic microscopy imager was 532 nm. The laser wavelength of the photoacoustic tomography imager was 750 and 850 nm. The vascular quantification was analyzed using the ImageJ (National Institutes of Health, Bethesda, USA) software.

2.12. Immunohistochemistry of the tumor tissue

To inspect the expression of HIF-1α and PD-1, 6 mice with 4T1 tumors were selected and divided into 2 groups [the control group and injection of Pt@PEG-Ce6 with 660 nm laser irradiation group (1 W/cm^2)]. After intravenous injection of 100 μL of Pt@PEG-Ce6 for 4 h, the tumor region of each mouse received laser irradiation (660 nm, 1 W/cm^2) for 5 min. Then, the tumor tissues were collected 24 h after the different treatments. Hematoxylin and eosin (H&E) staining of the major tumors was performed to observe the structures of the tumor tissues. Then, the tumor tissues were stained with HIF-1α and PD-1 antibodies, which were diluted 1:500 in 3% BSA blocking buffer. Finally, images were obtained with an Upright Metallurgical Microscope.

2.13. PDT effect of the Pt@PEG-Ce6 nanocomposite in vivo

Twenty-five mice with 4T1 tumors were selected and divided into 5 groups including saline, 660 nm laser irradiation, Pt@PEG-Ce6 without radiation, free Ce6 with 660 nm laser irradiation (1 W/cm^2), and Pt@PEG-Ce6 with 660 nm laser irradiation (1 W/cm^2). The final concentration of Ce6 was 0.5 mg/mL. After intravenous injection of 100 μL of Pt@PEG-Ce6 or free Ce6 for 4 h, the tumor region of each mouse received laser irradiation (660 nm, 1 W/cm^2) for 5 min. The tumor size of the mice in each group were measured every 2 days as length $\times$ (width)^2 $\times$ 1/2 with a caliper. The body weights were also measured. The relative tumor volume was calculated as V/V_0, where V_0 and V stand for the tumor volume on the first day and on the day of measurement, respectively. After 12 days, the heart, liver, spleen, lung, and kidney of each mouse were collected for histological analysis.

2.14. Statistical analysis

Experimental results were shown as the mean $\pm$ standard deviation. Statistical significance was performed by the analysis of variance test. $P < 0.05$ was considered to indicate a statistical difference.

3. Results

mPt were first synthesized using chloroplatinic acid as the precursor and ascorbic acid as the structure-directing agent. Transmission electron microscopy (TEM) and scanning electron microscopy (SEM) show that the mPt nanoparticles were porous in structure with a pore size of approximately 11 nm. The mPt nanoparticles have excellent dispersity and diagonal dimension of approximately 70 nm (Fig. 1A and B). To connect the photosensitizer Ce6 onto mesoporous Pt, the carboxy terminus of the Ce6 was connected to the amino terminus of the bifunctional SH-PEG-NH$_2$ *via* a condensation reaction, and then PEG-Ce6 was modified onto the mPt moiety *via* the mercapto terminal of SH-PEG-NH$_2$. The morphology of the prepared Pt@PEG-Ce6 particles was similar to that of the mPt nanoparticles (Fig. 1C). According to the energy-dispersive X-ray spectroscopy (EDX) results (Supporting Information Fig. S1), the mass ratio of Pt in the prepared Pt@PEG-Ce6 was approximately 85%. The zeta potentials of mPt and Pt@PEG-Ce6 were measured to be −16 and −18.5 mV, respectively (Fig. 1D), suggesting the successful modification with Ce6. The hydrodynamic diameters of mPt and Pt@PEG-Ce6 were measured to be 67 and 164 nm, respectively (Fig. 1E). Furthermore, the FTIR spectra of Pt@PEG-Ce6 displayed a C−O vibration peak at 1700 cm^{-1}, which indicated the successful conjugation of Ce6 (Fig. 1F). In addition, the UV−Vis absorption spectrum of the Pt@PEG-Ce6 nanocomposite showed characteristic absorption peaks of Ce6 at 400 and 660 nm (Fig. 1G). The loading content of Ce6 in the mPt nanoparticles was measured to be 13.4%, *w/w* (Supporting Information Fig. S2A and B). Pt@PEG-Ce6 showed good dispersion stability in physiological solutions, such as PBS and cell culture media including 10% fetal bovine serum (Fig. S2C). In addition, the *in vitro* CT images of mPt demonstrated a positive contrast enhancement in a dose-dependent manner (Fig. 1H). The CT values of mPt were proportional to the concentrations, showing the potential of mPt as a contrast material for CT imaging (Fig. S2D). In addition, the PA
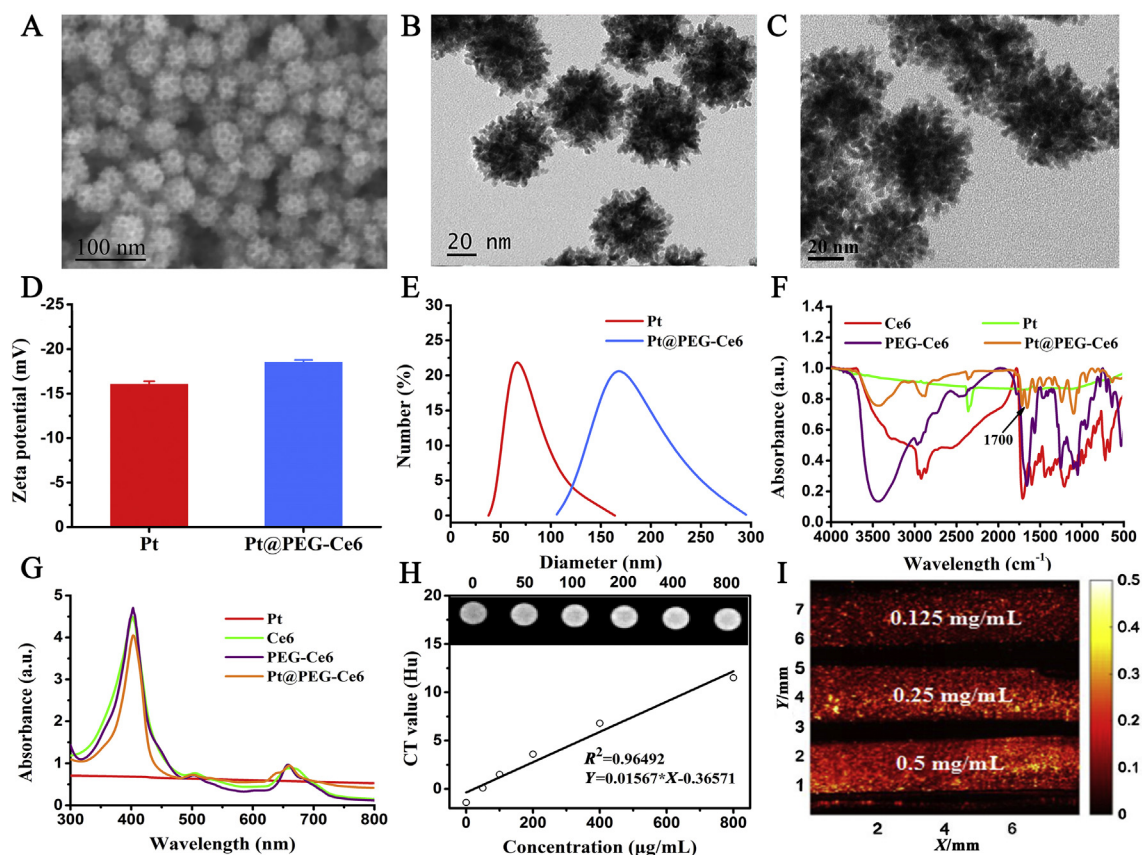
Figure 1 Characterization of the Pt@PEG-Ce6 nanoplatforms. (A) SEM image of mPt nanoparticles. (B) TEM image of mPt nanoparticles. (C) TEM image of Pt@PEG-Ce6. (D) Zeta potentials of mPt and Pt@PEG-Ce6. Data are presented as the mean $\pm$ SD ($n = 3$). (E) Hydrodynamic diameters of mPt and Pt@PEG-Ce6. (F) FT-IR spectra of mPt, Ce6, PEG-Ce6, and Pt@PEG-Ce6. (G) UV–Vis absorption spectra of mPt, Ce6, PEG-Ce6, and Pt@PEG-Ce6. (H) CT images and values of mPt nanomaterials at different concentrations. (I) Photoacoustic images of Pt@PEG-Ce6 nanomaterials at different concentrations.

signal of Pt@PEG-Ce6 increased at increasing concentrations (Fig. 1I), indicating its potential for PA imaging.

We tested the O_2 generation in the solutions of H_2O, H_2O_2, Pt + H_2O_2, Pt@PEG-Ce6+H_2O_2, and Ce6+H_2O_2. Oxygen bubbles were obviously observed in the Pt + H_2O_2 and Pt@PEG-Ce6+H_2O_2 solutions (Fig. 2A and B), suggesting that mPt catalyzes H_2O_2 to produce O_2. In the absence of the nanomaterials or H_2O_2, there was almost no oxygen generation. We then investigated the $^1O_2$ generation ability of Pt@PEG-Ce6 using DPBF as a probe. The absorption peaks of DPBF at 410 nm remained stable under laser irradiation at different times, and no $^1O_2$ was generated in this process (Fig. 2C). In contrast, the DPBF absorption at 410 nm gradually decreased with increasing irradiation time (660 nm laser, 1 W/cm^2) in the presence of Ce6 or Pt@PEG-Ce6, indicating that Ce6 and Pt@PEG-Ce6 were highly efficient in the generation of $^1O_2$ and that the $^1O_2$ production capacity of Pt@PEG-Ce6 was slightly higher than Ce6 over time. In addition, the ability of Pt@PEG-Ce6 to generate $^1O_2$ was higher in the presence of H_2O_2 than without H_2O_2, suggesting that Pt@PEG-Ce6 reacted with H_2O_2 to produce more O_2 to enhance the PDT effect.

The H_2O_2 concentration significantly increased in the tumor microenvironment, so Pt@PEG-Ce6 can react with endogenous H_2O_2 to produce O_2 *in situ* to improve PDT efficacy. We treated 4T1 cells and MCF-7/ADR (dox-resistant) cells with Pt@PEG-

Ce6 or free Ce6 in a nitrogen or air atmosphere and irradiated the cells with a laser (660 nm, 1 W/cm^2) for 10 min per well. The results showed that the Pt@PEG-Ce6 group had a stronger cell-killing effect than the free Ce6 group in both cell types, regardless of the air or nitrogen atmosphere (Fig. 2D and E, and Supporting Information Fig. S3). As the concentration increased, both Pt@PEG-Ce6 and Ce6 showed stronger cell-killing effects in air. In a nitrogen atmosphere, free Ce6 has a significantly lower cell-killing effect than in air, suggesting that Pt@PEG-Ce6 catalyzes hydrogen peroxide to generate oxygen in hypoxic tumor cells to promote the PDT effect.

Before applying Pt@PEG-Ce6 for *in vivo* experiments, we evaluated its biocompatibility. First, we tested its cytotoxicity at the cellular level. The viabilities of 4T1 and MCF-7/ADR (dox-resistant) cells incubated with mPt and Pt@PEG-Ce6 in the concentration range of 0–80 ppm were higher than 80%, demonstrating good biocompatibility (Supporting Information Fig. S4). We further investigated the biosafety of Pt@PEG-Ce6 *in vivo* to promote its therapeutic application in the tumor hypoxic microenvironment. First, BALB/c mice were injected intravenously with Pt@PEG-Ce6 (1 mg/mL), and the blood biochemistry parameters were analyzed after 24 h. The results showed that the blood biochemical indexes of the mice injected with Pt@PEG-Ce6 were not statistically different from those of healthy mice (Fig. 3A), demonstrating that Pt@PEG-Ce6 had no obvious toxicity. In
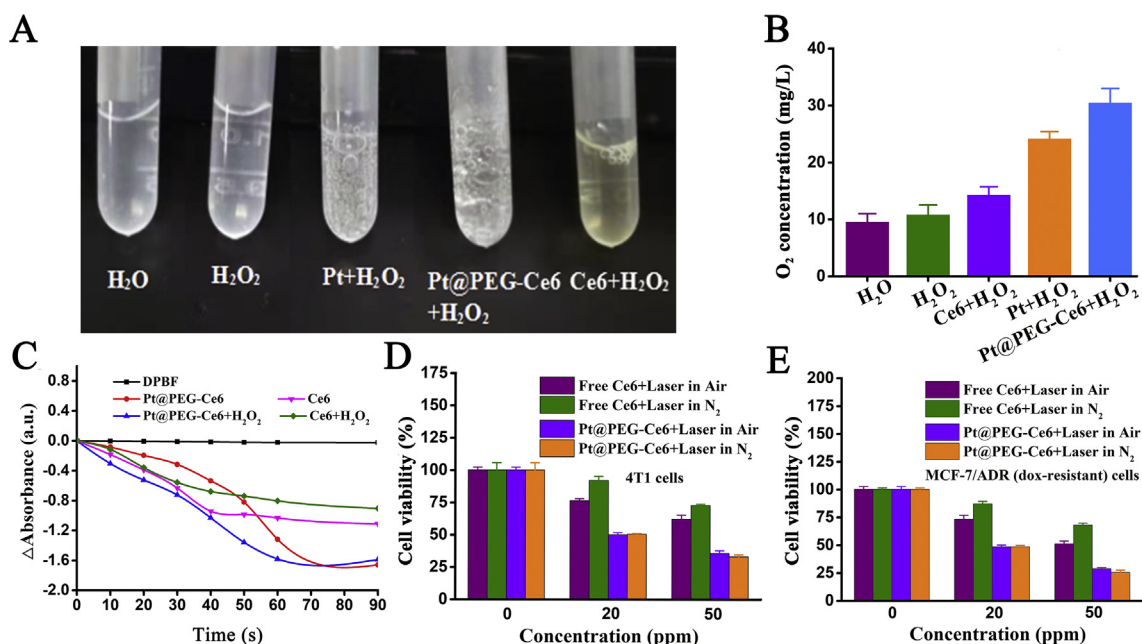
Figure 2 (A) Optical images of oxygen bubbles and (B) oxygen concentrations in the solutions of H_2O, H_2O_2, $Pt + H_2O_2$, Pt@PEG-Ce6+H_2O_2, and Ce6+H_2O_2 ($n = 3$). (C) Relative decay curves of DPBF absorption at 410 nm in Ce6 and Pt@PEG-Ce6 solutions with or without H_2O_2 after different irradiation times (660 nm, 1 W/cm^2). (D) Relative viabilities of 4T1 cells incubated with Ce6 or Pt@PEG-Ce6 at different concentrations after laser irradiation (660 nm, 1 W/cm^2, 10 min) in an air and nitrogen atmosphere ($n = 3$). (E) Relative viabilities of MCF-7/ADR (dox-resistant) cells incubated with Ce6 or Pt@PEG-Ce6 at different concentrations after laser irradiation (660 nm, 1 W/cm^2, 10 min) in an air and nitrogen atmosphere ($n = 3$). Data are presented as the mean $\pm$ SD.

addition, each group of mice was sacrificed after 24 h, and the main organs were harvested to stain with H&E to study the potential toxicity of Pt@PEG-Ce6. Compared with healthy mice, no obvious damage was found in the tissue sections of the mice injected with Pt@PEG-Ce6 (Fig. 3B), indicating that Pt@PEG-Ce6 has good biocompatibility.

Because Pt has CT imaging capability, the CT value of the tumor significantly increased after injecting 100 µL of Pt@PEG-Ce6 (1 mg/mL) into the mice (Fig. 4A and B and Supporting Information Fig. S5A and B), indicating that Pt@PEG-Ce6 can be used for CT imaging. Furthermore, we performed PA scanning on the tumor areas of the mice and compared the PA signals before and after injection of Pt@PEG-Ce6 (100 µL) and irradiation (660 nm, 1 W/cm^2, Fig. 4C–E, and Fig. S5C and D). As indicated by the yellow circles, the blood vessels in the tumor area of the mice decreased following treatment. To gain quantitative insight into change of blood vessels, the changes of vascular density were calculated with the real-time (RT) mode before and after treatment. After PDT, the tumor vessels were destroyed and the vascular density were reduced ($P < 0.05$), manifesting the vascular occlusion effect of Pt@PEG-Ce6. Moreover, as indicated by the white arrows, the signal of the tumor blood vessel was enhanced after injection of Pt@PEG-Ce6, indicating that Pt@PEG-Ce6 has the potential for PA imaging. In addition, the oxihemogram showed that the color level of the tumor area tends to be red after injection of Pt@PEG-Ce6, indicating an increase in oxygen saturation (SaO$_2$, Fig. 4F and G). This represented an increase in oxygen in the tumor area after treatment.

Pt@PEG-Ce6-based PDT can generate oxygen in the hypoxic microenvironment of the tumor. The expression level of HIF-1α is closely related to tumor hypoxia. Therefore, the detection of HIF-1α in tumors could reflect the degree of hypoxia of the tumor and further reflect the PDT effect. In addition, the PD-1 molecule is highly expressed in tumor-infiltrating lymphocytes, so it will be interesting to investigate whether our treatment would down-regulate the expression of PD-1 to suppress immune evasion. The immunohistochemical images and protein quantitative data showed that the expression levels of HIF-1α and PD-1 in the tumors of the mice treated with Pt@PEG-Ce6 for 24 h were lower than that of the mice injected with just saline ($P < 0.05$, Fig. 5A–C), which indicates that Pt@PEG-Ce6 can improve hypoxia and inhibit immune evasion in hypoxic solid tumors.

Because Pt@PEG-Ce6 can improve the *in vitro* PDT effect, we further applied Pt@PEG-Ce6 for *in vivo* tumor therapeutic efficacy. Accordingly, BALB/c model mice bearing a 4T1 tumor were divided into five groups ($n = 5$ per group), including saline, 660 nm laser irradiation, Pt@PEG-Ce6 without irradiation, free Ce6 with 660 nm laser irradiation (1 W/cm^2), and Pt@PEG-Ce6 with 660 nm laser irradiation (1 W/cm^2). The results are shown in Fig. 5E. The relative tumor volumes of the mice in the Pt@PEG-Ce6 with 660 nm laser irradiation group (1 W/cm^2, 5 min) were significantly inhibited compared to only the laser (1 W/cm^2, 5 min) or Pt@PEG-Ce6 groups over 12 days ($P < 0.05$). The group with intravenous injection of free Ce6 with 660 nm laser irradiation (1 W/cm^2, 5 min) only had a good inhibitory effect for the initial 10 days. This was attributed to the
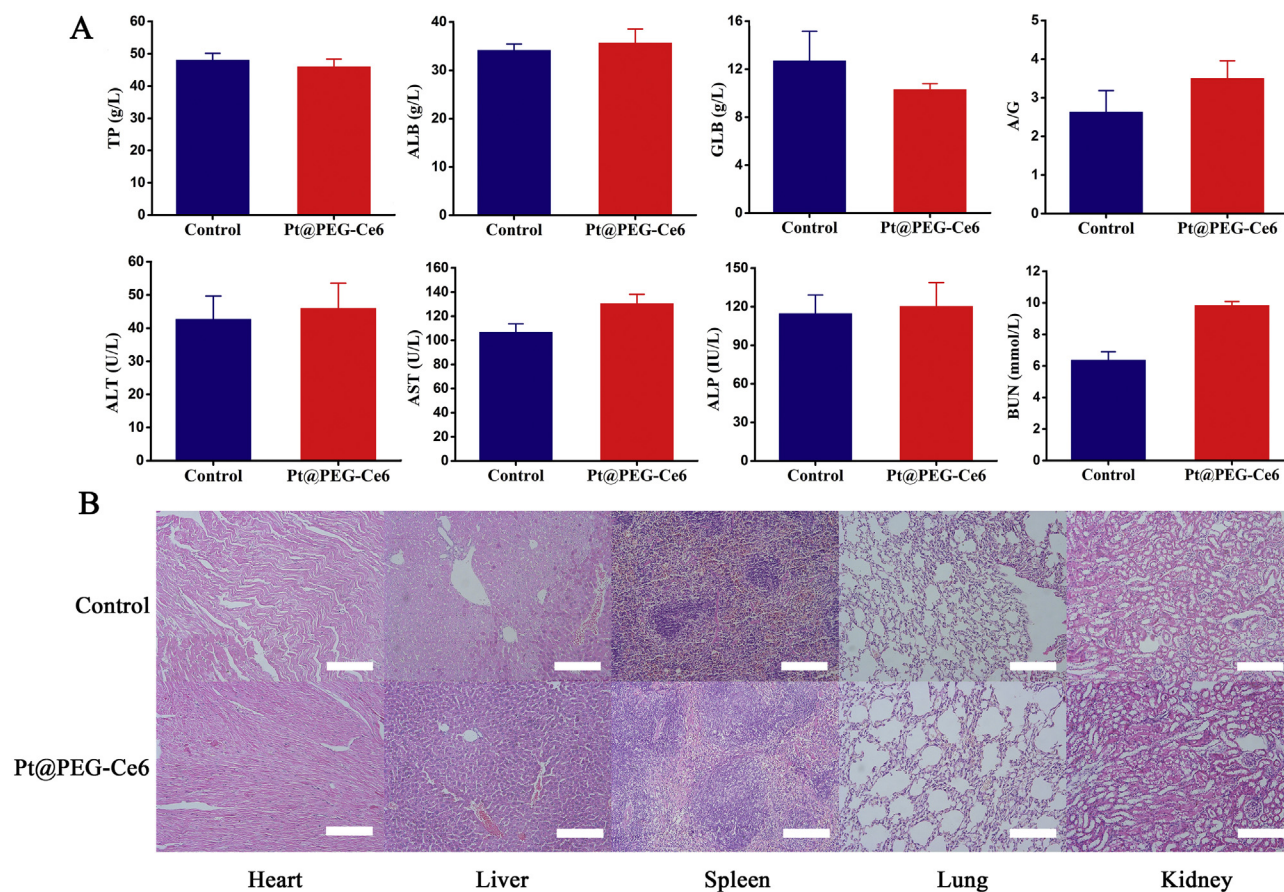
Figure 3 (A) Serum biochemistry results obtained from mice 24 h after injection with Pt@PEG-Ce6 and untreated mice ($n = 3$). Data are presented as the mean $\pm$ SD. (B) H&E images of the major organs of the mice from the control group and Pt@PEG-Ce6 group (scale bar, 100 μm).

oxygen generation capability of the nanocomposite *in situ* in the tumor areas, which enhanced the therapeutic effect of PDT. These results were further confirmed by representative tumor images on Day 12 (Fig. 5D). During the treatment period, there was no significant reduction in the bodyweights of the mice from all groups (Fig. 5F), and the organs of the mice that were cured had no abnormalities (Supporting Information Fig. S6).

4. Discussion

Hypoxia is an important feature of the solid tumor microenvironment, which plays an important role in tumor invasion, immune escape, metastasis, PDT and chemoradiotherapy resistance[33]. PDT is a promising noninvasive therapy with a low incidence of side effects. However, the loss of oxygen in the treatment itself and the hypoxic microenvironment inside the tumor significantly reduce the therapeutic effects of PDT[34]. Therefore, solving hypoxia is very important in enhancing the effects of PDT. Current methods to improve hypoxia include *in situ* oxygen-producing nanomaterials such as MnO_2[35,36]. The main problem with MnO_2 is the complex synthetic procedures, which limits its practical application[37,38]. In this work, we utilized mPt nanosphere as a carrier to synthesize a nanoparticle Pt@PEG-

Ce6 by covalently linking the Ce6. This novel mPt nanoplatform was designed that could catalyze the formation of O_2 and H_2O *in situ* without the introduction of a catalytic enzyme. As expected, this nanosystem can significantly increase ROS under laser irradiation for efficient PDT. We systematically investigated the properties of Pt@PEG-Ce6 *in vivo* and *in vitro*, including its ability to decompose hydrogen peroxide to produce oxygen, the singlet oxygen production capacity, biosafety evaluation, cellular uptake, blood circulation, tissue distribution, and imaging. Pt@PEG-Ce6 has the following advantages: (1) Pt@PEG-Ce6 has good catalase activity, which can react with H_2O_2 in the tumor site to generate O_2 *in situ* without additional catalytic enzyme and enhance the PDT effect; (2) Pt@PEG-Ce6 is able to generate more ROS upon irradiation to enhance the PDT effect; (3) Pt@PEG-Ce6 has good biocompatibility; (4) Pt@PEG-Ce6 has *in vivo* CT imaging ability, which provides good tracking for the visualization of tissue distribution; and (5) Pt@PEG-Ce6 is helpful for *in vivo* photoacoustic microscopy imaging, which can enhance the signal of the tumor blood vessels. The results showed that PDT based on Pt@PEG-Ce6 had a good occlusive effect on tumor microvessels to limit tumor progression. At the same time, photoacoustic tomography imaging realized the monitoring of the SaO_2 of tumor, and detected the increase of the SaO_2 of tumor after PDT.
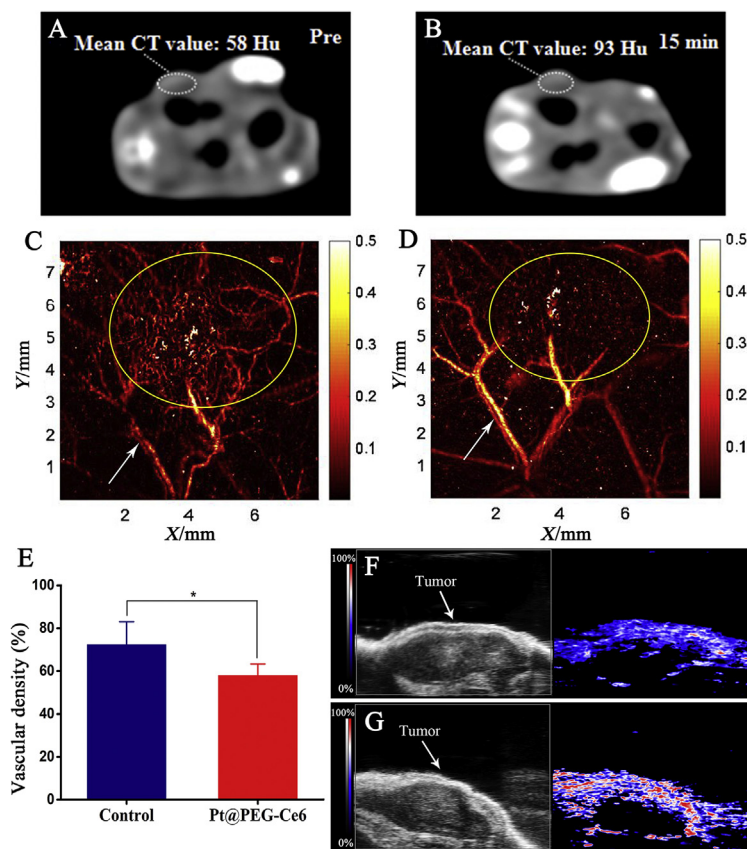
Figure 4 CT images of mice (A) before and (B) after injection of Pt@PEG-Ce6. Photoacoustic microscopy images of mice (C) before and (D) after injection of Pt@PEG-Ce6 and irradiation (660 nm, 1 W/cm^2). The arrows and circles indicate the blood vessels. (E) The vascular densities of tumors before and after injection of Pt@PEG-Ce6 and irradiation (660 nm, 1 W/cm^2) ($n = 3$). Data are presented as the mean $\pm$ SD. $^*P < 0.05$ *vs.* the control group. Photoacoustic tomography images (F) before and (G) after injection of Pt@PEG-Ce6 and irradiation (660 nm, 1 W/cm^2).

HIF-1 is a transcription factor that is stable under hypoxic conditions and is mainly composed of oxygen-regulated subunits (HIF-1α) and oxygen-independent subunits (HIF-1β). HIF-1α is regulated by hypoxic signaling, which plays an important role in angiogenesis, immune escape, metastasis, chemoradiotherapy resistance and restriction of PDT[39–42]. Under hypoxic conditions, the increase in HIF-1α induces VEGF expression, and the dendritic cell (DC) response to tumor-derived VEGF increases the expression of PD-L1[42,43]. At the same time, HIF-1α can also selectively upregulate PD-L1 on tumor cells by directly binding to the hypoxia response element in the proximal promoter of PD-L1. When PD-1, a glycosylated protein on the T-cell surface, binds to its ligand PD-L1, it will inhibit the transcription and translation of genes and cytokines required for T-cell activation and exerts negative regulation on T-cell activity, thereby inhibiting the body's anti-tumor immunity and leading to the occurrence of tumor immune escape[44,45]. In our study, PDT based on Pt@PEG-Ce6 can effectively inhibit the expression of HIF-1α. The inhibition of HIF-1α can reduce the expression of PD-L1, thus inhibiting combination of PD-L1 and PD-1, and activating the tumor-killing effect of the immune effector cells to avoid immune escape. In addition, some studies have found that PDT can increase the T-cell

infiltration into the tumor and induce immunogenic cell death (ICD) in tumor cells to activate immunity, thus promoting T-cell proliferation[46]. The host immune boost might be limited with PDT alone because of the immunosuppressive environment in tumor[47], the improvement of tumor hypoxia and PDT together activated the expression of immune cells, thus reducing the expression of PD-1. We found for the first time that PDT based on Pt@PEG-Ce6 can reduce the expression of PD-1 on tumor infiltrating lymphocytes. This is very interesting and we will do further research to discuss the mechanism.

5. Conclusions

We constructed an ingenious Pt@PEG-Ce6 nanoplatform that can generate ROS *in situ* without the additional introduction or loading of catalytic enzymes to enhance PDT. Cellular experiments and *in vivo* tests in the 4T1 mouse model confirmed that Pt@PEG-Ce6 can generate oxygen to fight against the hypoxic microenvironment of breast cancer and enhance the effect of PDT. Additionally, the preliminary imaging results support its potential for CT and PA imaging. Moreover, Pt@PEG-Ce6 can influence
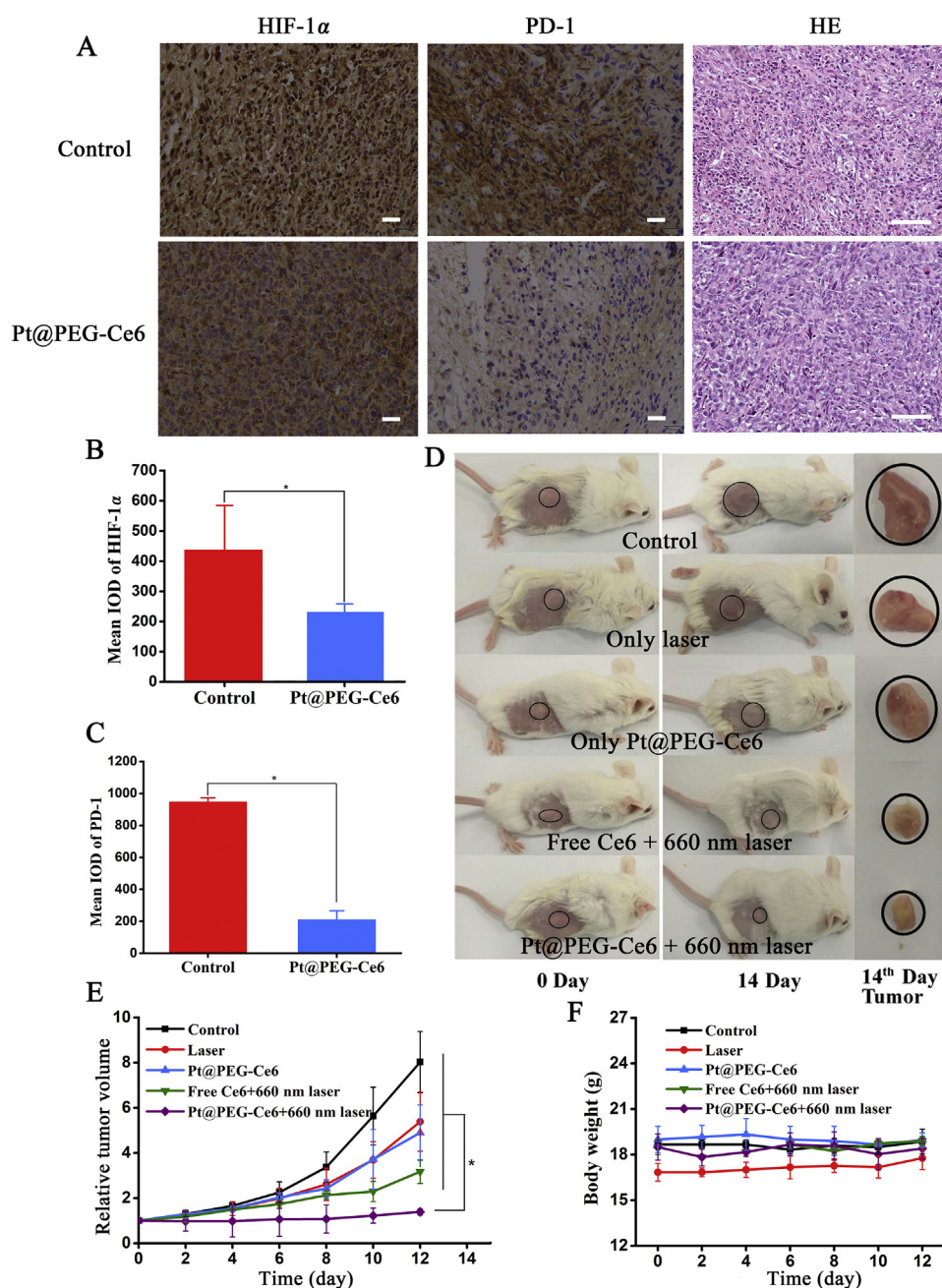
Figure 5 (A) Immunohistochemistry images of tumor slices stained for HIF-1α and PD-1 after intravenous injection of PBS and Pt@PEG-Ce6 (scale bar, 100 μm). (B) and (C) Quantification of the integrated option density from (A) ($n = 3$). Data are presented as the mean $\pm$ SD. $^*P < 0.05$ vs. the control group. (D) Tumor changes of mice before and after treatment. (E) Tumor volume changes of the mice treated with different ways ($n = 5$). Data are presented as the mean $\pm$ SD. $^*P < 0.05$ vs. the control group, laser group, Pt@PEG-Ce6 group, and free Ce6+660 nm group. (F) Body weights of the mice from different groups ($n = 5$). Data are presented as the mean $\pm$ SD.

the expression of HIF-1a and PD-1 in animals, verifying that Pt@PEG-Ce6 can indirectly play a role in tumor treatment by regulating the body's immunity.

Author contributions

Lingyan Zhang, Zhaogang Teng, and Guangming Lu designed the research. Mifang Li carried out the experiments and performed data analysis. Meng Dang, Yuxia Tang and Shouju Wang participated part of the experiments. Quan Zhou provided experimental drugs and quality control. Mifang Li and Lingyan Zhang wrote the manuscript. Zhaogang Teng and Jijun Fu revised the manuscript. All of the authors have read and approved the final manuscript.

Conflicts of interest

The authors have no conflicts of interest to declare.

Appendix A.   Supporting information

Supporting data to this article can be found online at https://doi.org/10.1016/j.apsb.2020.05.003.

References

1. Kwiatkowski S, Knap B, Przystupski D, Saczko J, Kędzierska E, Knap-Czop K, et al. Photodynamic therapy—mechanisms, photosensitizers and combinations. *Biomed Pharmacother* 2018;**106**: 1098−107.
2. Sarcan ET, Silindir-Gunay M, Ozer AY. Theranostic polymeric nanoparticles for NIR imaging and photodynamic therapy. *Int J Pharm* 2018;**551**:329−38.
3. Parks SK, Cormerais Y, Pouysségur J. Hypoxia and cellular metabolism in tumor pathophysiology. *J Physiol* 2017;**598**:2439−50.
4. Graham K, Unger E. Overcoming tumor hypoxia as a barrier to radiotherapy, chemotherapy and immunotherapy in cancer treatment. *Int J Nanomed* 2018;**13**:6049−58.
5. Kim JY, Lee JY. Targeting tumor adaption to chronic hypoxia: implications for drug resistance, and how it can be overcome. *Int J Mol Sci* 2017;**18**:e1854.
6. Lee CT, Boss MK, Dewhirst MW. Imaging tumor hypoxia to advance radiation oncology. *Antioxidants Redox Signal* 2014;**21**:313−37.
7. Dang J, He H, Chen D, Yin L. Manipulating tumor hypoxia toward enhanced photodynamic therapy (PDT). *Biomater Sci* 2017;**5**: 1500−11.
8. Sun YX, Zhao DY, Wang G, Wang Y, Cao LL, Sun J, et al. Recent progress of hypoxia-modulated multifunctional nanomedicines to enhance photodynamic therapy: opportunities, challenges, and future development. *Acta Pharm Sin B* 2020. Available from: https://doi.org/10.1016/j.apsb.2020.01.004.
9. Li J, Huang J, Ao Y, Li S, Miao Y, Yu Z, et al. Synergizing upconversion nanophotosensitizers with hyperbaric oxygen to remodel the extracellular matrix for enhanced photodynamic cancer therapy. *ACS Appl Mater Interfaces* 2018;**10**:22985−96.
10. Plenagl N, Duse L, Seitz BS, Goergen N, Pinnapireddy SR, Jedelska J, et al. Photodynamic therapy—hypericin tetraether liposome conjugates and their antitumor and antiangiogenic activity. *Drug Deliv* 2019;**26**:23−33.
11. Lamberti MJ, Morales Vasconsuelo AB, Chiaramello M, Ferreira VF, Oliveira MM, Ferreira SB, et al. NQO1 induction mediated by photodynamic therapy synergizes with β-Lapachone-halogenated derivative against melanoma. *Biomed Pharmacother* 2018;**108**: 1553−64.
12. Tao D, Feng L, Chao Y, Liang C, Song X, Wang H, et al. Covalent organic polymers based on fluorinated porphyrin as oxygen nanoshuttles for tumor hypoxia relief and enhanced photodynamic therapy. *Adv Funct Mater* 2018;**28**:1804901.
13. Gao M, Liang C, Song X, Chen Q, Jin Q, Wang C, et al. Erythrocyte-membrane-enveloped perfluorocarbon as nanoscale artificial red blood cells to relieve tumor hypoxia and enhance cancer radiotherapy. *Adv Mater* 2017;**35**:1701429.
14. Revuri V, Cherukula K, Nafiujjaman M, Vijayan V, Jeong YY, Park IK, et al. *In situ* oxygenic nanopods targeting tumor adaption to hypoxia potentiate image-guided photothermal therapy. *ACS Appl Mater Interfaces* 2019;**11**:19782−92.
15. He Z, Huang X, Wang C, Li X, Liu Y, Zhou Z, et al. A catalase-like metal-organic framework nanohybrid for O_2-evolving synergistic chemoradiotherapy. *Angew Chem Int Ed Engl* 2019;**58**: 8752−6.
16. Maji SK, Yu S, Chung K, Ramasamy MS, Lim JW, Wang J, et al. Synergistic nanozymetic activity of hybrid gold bipyramid-molybdenum disulfide core@shell nanostructures for two-photon imaging and anticancer therapy. *ACS Appl Mater Interfaces* 2018;**10**: 42068−76.
17. Chen Q, Feng L, Liu J, Zhu W, Dong Z, Wu Y, et al. Intelligent albumin-MnO_2 nanoparticles as pH-/H_2O_2-responsive dissociable nanocarriers to modulate tumor hypoxia for effective combination therapy. *Adv Mater* 2016;**28**:7129−36.
18. Song M, Liu T, Shi C, Zhang X, Chen X. Bioconjugated manganese dioxide nanoparticles enhance chemotherapy response by priming tumor-associated macrophages toward M1-like phenotypeand attenuating tumor hypoxia. *ACS Nano* 2016;**10**:633−47.
19. Lin T, Zhao X, Zhao S, Yu H, Cao W, Chen W, et al. O_2-generating MnO_2 nanoparticles for enhanced photodynamic therapy of bladder cancer by ameliorating hypoxia. *Theranostics* 2018;**8**:990−1004.
20. Lim B, Jiang M, Camargo PH, Cho EC, Tao J, Lu X, et al. Pd-Pt bimetallic nanodendrites with high activity for oxygen reduction. *Science* 2009;**324**:1302−5.
21. Zhang L, Jia H, Liu C, Liu M, Meng Q, He W. Enhanced generation of reactive oxygen species and photocatalytic activity by Pt-based metallic nanostructures: the composition matters. *J Environ Sci Health C Environ Carcinog Ecotoxicol Rev* 2019;**37**:1−13.
22. Lin R, Cai X, Zeng H, Yu Z. Stability of high-performance Pt-based catalysts for oxygen reduction reactions. *Adv Mater* 2018;**30**: e1705332.
23. Wang X, Chang Z, Nie X, Li Y, Hu Z, Ma J, et al. A conveniently synthesized Pt (IV) conjugated alginate nanoparticle with ligand self-shielded property for targeting treatment of hepatic carcinoma. *Nanomedicine* 2019;**15**:153−63.
24. Wei J, Li J, Sun D, Li Q, Ma JY, Chen XL, et al. A novel theranostic nanoplatform based on Pd@Pt-PEG-Ce6 for enhanced photodynamic therapy by modulating tumor hypoxia microenvironment. *Adv Funct Mater* 2018;**28**:1706310.
25. Xu S, Zhu X, Zhang C, Huang W, Zhou Y, Yan D. Oxygen and Pt(II) self-generating conjugate for synergistic photo-chemo therapy of hypoxic tumor. *Nat Commun* 2018;**1**:2053.
26. Chu CH, Cheng SH, Chen NT, Liao WN, Lo LW. Microwave-synthesized platinum-embedded mesoporous silica nanoparticles as dual-modality contrast agents: computed tomography and optical imaging. *Int J Mol Sci* 2019;**20**:E1560.
27. Liu X, Zhang B, Fei B, Chen X, Zhang J, Mu X. Tunable and selective hydrogenation of furfural to furfuryl alcohol and cyclopentanone over Pt supported on biomass-derived porous heteroatom doped carbon. *Faraday Discuss* 2017;**202**:79−98.
28. Qi L, Cheng B, Yu J, Ho W. High-surface area mesoporous Pt/TiO_2 hollow chains for efficient formaldehyde decomposition at ambient temperature. *J Hazard Mater* 2016;**301**:522−30.
29. Jiang B, Li C, Malgras V, Imura M, Tominaka S, Yamauchi Y. Mesoporous Pt nanospheres with designed pore surface as highly active electrocatalyst. *Chem Sci* 2016;**7**:1575−81.
30. Salehi F, Daneshvar F, Karimi M, Dehdari Vari R, Mosleh-Shirazi MA, Sattarahmady N. Ehanced melanoma cell-killing by combined phototherapy/radiotherapy using a mesoporous platinum nanostructure. *Photodiagnosis Photodyn Ther* 2019;**28**:300−7.
31. Yu W, Batchelor-McAuley C, Chang X, Young NP, Compton RG. Porosity controls the catalytic activity of platinum nanoparticles. *Phys Chem Chem Phys* 2019;**21**:20415−21.

32. Dai X, Pi G, Yang SL, Chen GG, Liu LP, Dong HH. Association of PD-L1 and HIF-1α coexpression with poor prognosis in hepatocellular carcinoma. *Transl Oncol* 2018;**11**:559−66.

33. Bhandari V, Hoey C, Liu LY, Lalonde E, Ray J, Livingstone J, et al. Tumor oxygenation and hypoxia-inducible-factor-1 functional inhibition *via* a reactive-oxygen-species responsive nanoplatform for enhancing radiation therapy and abscopal effects. *ACS Nano* 2018;**12**: 8308−22.

34. Guo X, Qu J, Zhu C, Li W, Luo L, Yang J, et al. Synchronous delivery of oxygen and photosensitizer for alleviation of hypoxia tumor microenvironment and dramatically enhanced photodynamic therapy. *Drug Deliv* 2018;**25**:585−99.

35. Kim J, Cho HR, Jeon H, Kim D, Song C, Lee N, et al. Continuous O_2-evolving $MnFe_2O_4$ nanoparticle-anchored mesoporous silica nanoparticles for efficient photodynamic therapy in hypoxic cancer. *J Am Chem Soc* 2017;**139**:10992−5.

36. Zhu P, Chen Y, Shi J. Nanoenzyme-augmented cancer sonodynamic therapy by catalytic tumor oxygenation. *ACS Nano* 2018;**4**:3780−95.

37. Yao Y, Li N, Zhang X, Ong'achwa Machuki J, Yang D, Yu Y, et al. DNA-templated silver nanocluster/porphyrin/MnO_2 platform for label-free intracellular Zn^{2+} imaging and fluorescence-/magnetic resonance imaging-guided photodynamic therapy. *ACS Appl Mater Interfaces* 2019;**11**:13991−4003.

38. Wang X, Dai J, Wang X, Hu Q, Huang K, Zhao Z, et al. MnO_2-DNA zyme-photosensitizer nanocomposite with AIE characteristic for cell imaging and photodynamic-gene therapy. *Talanta* 2019;**202**:591−9.

39. Barker HE, Paget JTE, Khan AA, Harrington KJ. The tumour microenvironment after radiotherapy: mechanisms of resistance and recurrence. *Nat Rev Canc* 2015;**15**:409−25.

40. Subarsky P, Hill RP. The hypoxic tumour microenvironment and metastatic progression. *Clin Exp Metastasis* 2003;**20**:237−50.

41. Olivier Trédan, Galmarini CM, Patel K, Tannock IF. Drug resistance and the solid tumor microenvironment. *J Natl Cancer Inst* 2007;**99**:1441−54.

42. Barsoum IB, Koti M, Siemens DR, Graham CH. Mechanisms of hypoxia-mediated immune escape in cancer. *Canc Res* 2014;**74**:7185−90.

43. Xue S, Hu M, Li P, Ma J, Xie L, Teng F, et al. Relationship between expression of PD-L1 and tumor angiogenesis, proliferation, and invasion in glioma. *Oncotarget* 2017;**8**:49702−12.

44. Noman MZ, Desantis G, Janji B, Hasmim M, Karray S, Dessen P, et al. PD-L1 is a novel direct target of HIF-1, and its blockade under hypoxia enhanced MDSC-mediated T cell activation. *J Exp Med* 2014; **211**:781−90.

45. Kumar S, Sharawat SK. Epigenetic regulators of programmed death-ligand 1 expression in human cancers. *Transl Res* 2018;**202**:129−45.

46. Nath S, Obaid G, Hasan T. The course of immune stimulation by photod1ynamic therapy: bridging fundamentals of photochemically induced immunogenic cell death to the enrichment of T-cell repertoire. *Photochem Photobiol* 2019;**95**:1288−305.

47. Yu W, He X, Yang Z, Yang X, Xiao W, Liu R, et al. Sequentially responsive biomimetic nanoparticles with optimal size in combination with checkpoint blockade for cascade synergetic treatment of breast cancer and lung metastasis. *Biomaterials* 2019;**217**:119309.